Supplementary Information

Tuning ORR on Graphene-MN_4 Single-Atom Sites via 2D TMD Coupling

Yue Dong, Zheng-Zhe Lin*

School of Physics, Xidian University, Xi'an 710071, China

* Corresponding Author. E-mail address: zzlin@xidian.edu.cn

1. The comparison of PBE and r^{2}SCAN functionals

To ensure the reliability of the chosen exchange-correlation functional, we performed benchmark calculations comparing the standard GGA functional (PBE-D4) with the more advanced meta-GGA functional (r^{2}SCAN-rVV10) on a representative system, including pristine FeN_4, CoN_4, MnN_4, and typical coupled systems such as FeN_4@WSe_2 and CoN_4@WSe_2. The calculation Gibbs free energies for ORR are plotted in **Fig. S1**. Although r^{2}SCAN-rVV10 predicts slightly weaker binding strengths for the ORR intermediates compared to PBE-D4, the overall reaction trends and the determination of the potential-limiting step remain unchanged. This consistency confirms that the PBE-D4 functional captures the essential physics of these systems and provides robust energetic descriptions for the catalytic mechanism. Therefore, subsequent mechanism analyses in this work are based on the PBE-D4 results with lower computational costs.

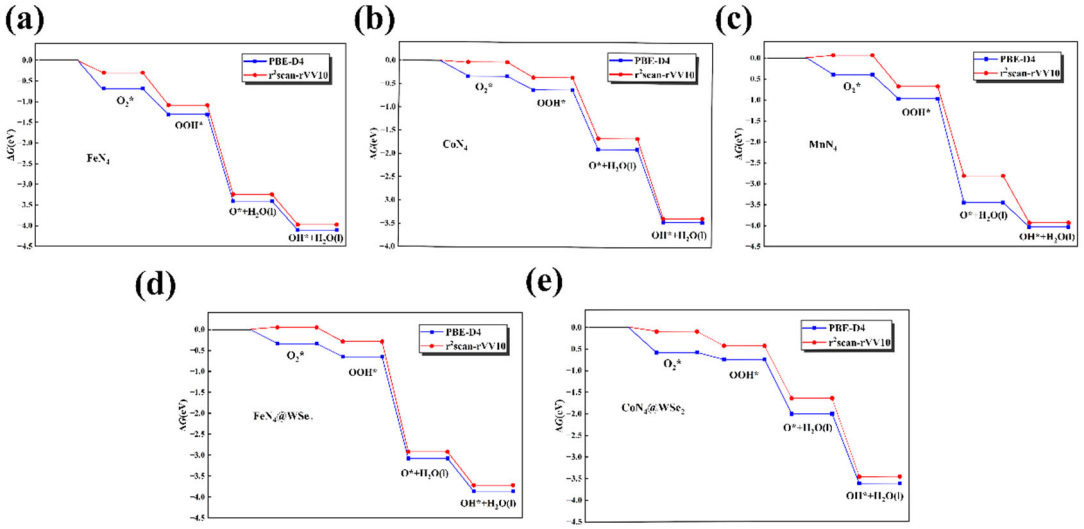

Fig. S1 Comparison of ORR Gibbs free energy diagrams calculated using PBE-D4 and r2SCAN-RVV10 for **(a)** FeN_4, **(b)** CoN_4, **(c)** MnN_4, **(d)** FeN_4@WSe_2, and **(e)** CoN_4@WSe_2.

Table S1 Comparison of Adsorption Free Energies Δ*G*

FeN_4	Δ*G* (PBE-D4)	Δ*G* (r^2SCAN-rVV10)
O_2*	-0.68	-0.30
OOH*	-1.30	-1.08
O*	-3.40	-3.24
OH*	-4.10	-3.97

CoN_4	Δ*G* (PBE-D4)	Δ*G* (r^2SCAN-rVV10)
O_2*	-0.33	-0.03
OOH*	-0.62	-0.35
O*	-1.89	-1.66
OH*	-3.45	-3.37

MnN_4	Δ*G* (PBE-D4)	Δ*G* (r^2SCAN-rVV10)
O_2*	-0.39	0.06
OOH*	-0.96	-0.67
O*	-3.45	-2.81
OH*	-4.03	-3.93

FeN_4@WSe_2	Δ*G* (PBE-D4)	Δ*G* (r^2SCAN-rVV10)
O_2*	-0.33	0.05
OOH*	-0.64	-0.28
O*	-3.07	-2.91
OH*	-3.85	-3.71

CoN_4@WSe_2	Δ*G* (PBE-D4)	Δ*G* (r^2SCAN-rVV10)
O_2*	-0.58	-0.09
OOH*	-0.74	-0.43
O*	-2.00	-1.64
OH*	-3.62	-3.46

The use of r^2SCAN-rVV10 serves as an important cross-validation of the PBE-D4 results. Although the free energies differ slightly, the consistent energetic trends across intermediates confirm the robustness of the computational predictions. These benchmark comparisons justify the use of PBE-D4 for large-scale screening across MN_4@RX_2 systems in the main text.

2. The adsorption energy of 3*d* transition metal atoms on the graphene–N_4 skeleton

To evaluate the stability of the MN_4 single-atom configurations, two complementary stability descriptors were considered, including the adsorption energy relative to isolated metal atoms and the formation energy referenced to bulk metal phases.

First, the anchoring stability of individual metal atoms (Sc, Ti, V, Cr, Mn, Fe, and Co) on the graphene–N_4 framework was evaluated using the adsorption energy, defined as

$$E_{ad}(M) = E(\text{graphene-}MN_4) - E(\text{graphene-}N_4) - E(M)$$

where, E(graphene-MN_4), E(graphene-N_4), and E(M) represent the total energies of the MN_4 structure, the pristine graphene-N_4 substrate, and an isolated metal atom, respectively. As summarized in **Table S2**, all calculated adsorption energies are strongly negative, indicating that the metal atoms can be firmly anchored at the N_4 coordination sites. Among them, TiN_4 and ScN_4 exhibit the strongest metal-substrate interactions, suggesting excellent anchoring stability.

Table S2 The adsorption energy of metal atoms on the graphene-N_4 skeleton.

	Sc	Ti	V	Cr	Mn	Fe	Co
E_{ad} (eV)	-8.41	-8.48	-7.77	-6.92	-6.65	-7.86	-8.03

Furthermore, to assess the thermodynamic stability of the single-atom configurations against metal aggregation, the formation energies referenced to bulk metal phases (E_{form}) were additionally calculated:

$$E_{form}(M) = E(\text{graphene-}MN_4) - E(\text{graphene-}N_4) - \mu_M^{bulk}$$

where μ_M^{bulk} represents the chemical potential of the corresponding bulk metal (Note: The thermodynamically stable phase of Mn is α-Mn. However, due to highly complex crystal structure, the bcc phase was adopted as the reference structure.). The calculated results in **Table S3** show that all MN_4 systems possess negative formation energies

relative to bulk metals, indicating that the isolated metal centers are thermodynamically favored over aggregation into metallic clusters.

Overall, the isolated-atom adsorption energies and bulk-referenced formation energies consistently demonstrate the robust stability of the MN_4 single-atom configurations, confirming both strong anchoring ability and favorable anti-clustering characteristics.

Table S3 Formation energies of MN_4 structures relative to bulk metal phases.

	Sc (hcp)	Ti (hcp)	V (bcc)	Cr (bcc)	Mn (bcc)	Fe (bcc)	Co (hcp)
E_{form} (eV)	-3.74	-2.75	-2.09	-2.43	-2.85	-2.65	-2.09

3. ORR Gibbs free energy of transition metals on N_4 skeleton

The Gibbs free energy (ΔG) of each reaction intermediate involved in ORR was calculated using the computational hydrogen electrode model. The corresponding reaction steps include O_2*, OOH*, O*, and OH* intermediates.

$$\Delta G = \Delta E + \Delta E_{ZPE} - T\Delta S + eU + \Delta G_{pH}$$

where ΔE, ΔE_{ZPE}, and ΔS are the changes of total energy, zero-point energy, and entropy, respectively; T = 298.15 K; eU represents the electrode potential correction, and $\Delta G_{pH} = k_B T \ln 10 \times$ pH accounts for the pH correction (pH = 0 in this work). The calculated values (**Table S4**) reveal that FeN_4, CoN_4, and MnN_4 exhibit more favorable free energy steps closer to the ideal thermodynamic pathway, suggesting superior ORR catalytic activity compared with ScN_4, TiN_4, and CrN_4.

Table S4 Gibbs free energy of 3*d* transition metal atoms related to ORR on the graphene-N_4 skeleton.

	Sc	Ti	V	Cr	Mn	Fe	Co
$\Delta G(O_2*)$	-2.81	-3.05	-2.76	-1.26	-0.63	-0.68	-0.46
ΔG(OOH*)	-4.99	-4.41	-4.22	-6.65	-1.50	-1.30	-0.87
ΔG(O*)	-	-6.72	-6.58	-	-3.55	-3.40	-2.15
ΔG(OH*)	-	-6.92	-6.12	-	-4.19	-4.10	-3.66
$\Delta G(H_2O)$	-	-4.92	-4.92	-	-4.92	-4.92	-4.92

4. Overpotential of MN_4 and its coupled RX_2 substrate

The theoretical ORR overpotential is determined from the potential-determining step (PDS):

$$\eta = \frac{\max(\Delta G)}{e} - 1.23\text{V}$$

The PBE-D4 calculations provide the reaction free energy ΔG (the data are listed in **Table S5**). The ORR overpotential on MN_4 and MN_4@RX_2 substrate is listed in **Table S6**, and the red font marks the lowest overpotential of the MN_4 system.

Table S5 Gibbs free energy for the oxygen reduction reaction (ORR) on graphene-supported MN_4 single-atom catalysts with different transition metal centers.

FeN_4@	MoS_2	$MoSe_2$	$MoTe_2$	MoSSe	WS_2	WSe_2	WTe_2	WSSe
$\Delta G(O_2*)$	-0.52	-0.56	-0.54	-0.58	-0.52	-0.39	-0.55	-0.60
ΔG(OOH*)	-1.21	-1.31	-1.09	-1.23	-1.18	-0.84	-1.12	-1.25
ΔG(O*)	-3.27	-3.26	-3.31	-3.31	-3.25	-2.70	-3.33	-3.33
ΔG(OH*)	-3.98	-4.06	-4.05	-4.02	-3.99	-3.91	-4.05	-4.01
$\Delta G(H_2O)$	-4.92	-4.92	-4.92	-4.92	-4.92	-4.92	-4.92	-4.92

CoN_4@	MoS_2	$MoSe_2$	$MoTe_2$	MoSSe	WS_2	WSe_2	WTe_2	WSSe
$\Delta G(O_2*)$	-0.27	-0.55	-0.49	0.88	-0.42	-0.58	-0.54	-0.53
ΔG(OOH*)	-1.26	-0.92	-0.91	-0.84	-0.88	-1.00	-0.89	-0.89
ΔG(O*)	-1.99	-2.20	-2.15	-2.05	-2.08	-2.22	-2.12	-2.14
ΔG(OH*)	-3.87	-3.80	-3.72	-3.65	-3.71	-3.82	-3.75	-3.75
$\Delta G(H_2O)$	-4.92	-4.92	-4.92	-4.92	-4.92	-4.92	-4.92	-4.92

MnN_4@	MoS_2	$MoSe_2$	$MoTe_2$	MoSSe	WS_2	WSe_2	WTe_2	WSSe
$\Delta G(O_2*)$	-0.43	-0.46	-0.56	-0.46	-0.41	-0.44	-0.55	-0.61
ΔG(OOH*)	-1.08	-1.31	-0.97	-1.08	-1.10	-1.10	-1.16	-1.38
ΔG(O*)	-3.30	-3.29	-3.44	-3.36	-3.38	-3.38	-3.44	-3.43
ΔG(OH*)	-4.12	-4.02	-4.09	-4.17	-4.10	-4.07	-4.07	-4.05
$\Delta G(H_2O)$	-4.92	-4.92	-4.92	-4.92	-4.92	-4.92	-4.92	-4.92

Table S6 ORR Overpotential on MN_4 and $MN_4@RX_2$.

@	-	MoS_2	$MoSe_2$	$MoTe_2$	MoSSe	WS_2	WSe_2	WTe_2	WSSe
FeN_4	0.53	0.54	0.43	0.48	0.53	0.49	0.38	0.51	0.55
CoN_4	0.35	0.49	0.30	0.31	0.38	0.34	0.22	0.33	0.33
MnN_4	0.58	0.43	0.49	0.58	0.48	0.50	0.54	0.59	0.60

5. Molecular dynamics simulations for $FeN_4@WSe_2$ and $CoN_4@WSe_2$

To verify the thermal stabilities of $FeN_4@WSe_2$ and $CoN_4@WSe_2$, molecular dynamics (MD) simulations were performed at 300 K. The Nosé-Hoover thermostat was employed to control the temperature.

The results for $FeN_4@WSe_2$ are shown in **Fig. S2(a)**. The simulation time step is set 0.5 fs. The total energy exhibits reasonable fluctuations around the average value, indicating that the system has reached equilibrium. During the simulation process, the FeN_4 group continuously deviates from its original position and then moves back. Root mean square displacement (RMSD)

$$\text{RMSD} = \sqrt{\frac{\sum |\vec{r}_i - \vec{r}_{i0}|^2}{N}}$$

shows reasonable fluctuations, indicating that the system is stable.

The results for $CoN_4@WSe_2$ are shown in **Fig. S2(b)**. Due to the relatively flat potential energy surface in the *xy*-plane, the simulation time step is set 0.2 fs to avoid errors. During the simulation process, CoN_4 with its graphene framework continuously drifts in the *xy*-plane, while its distance to WSe_2 substrate in the *z* direction keeps fluctuating. Root mean square displacement of the *z* direction (*z*-RMSD)

$$\text{z-RMSD} = \sqrt{\frac{\sum |z_i - z_{i0}|^2}{N}}$$

shows reasonable fluctuations, indicating that the graphene-WSe_2 interlayer distance is stable. Our simulation model is small. For real large graphene covering on WSe_2, the interlayer binding, which is proportional to its area, is large enough to compete with the

t

r

a

$\frac{1}{2}kT$ in the *xy*-plane.

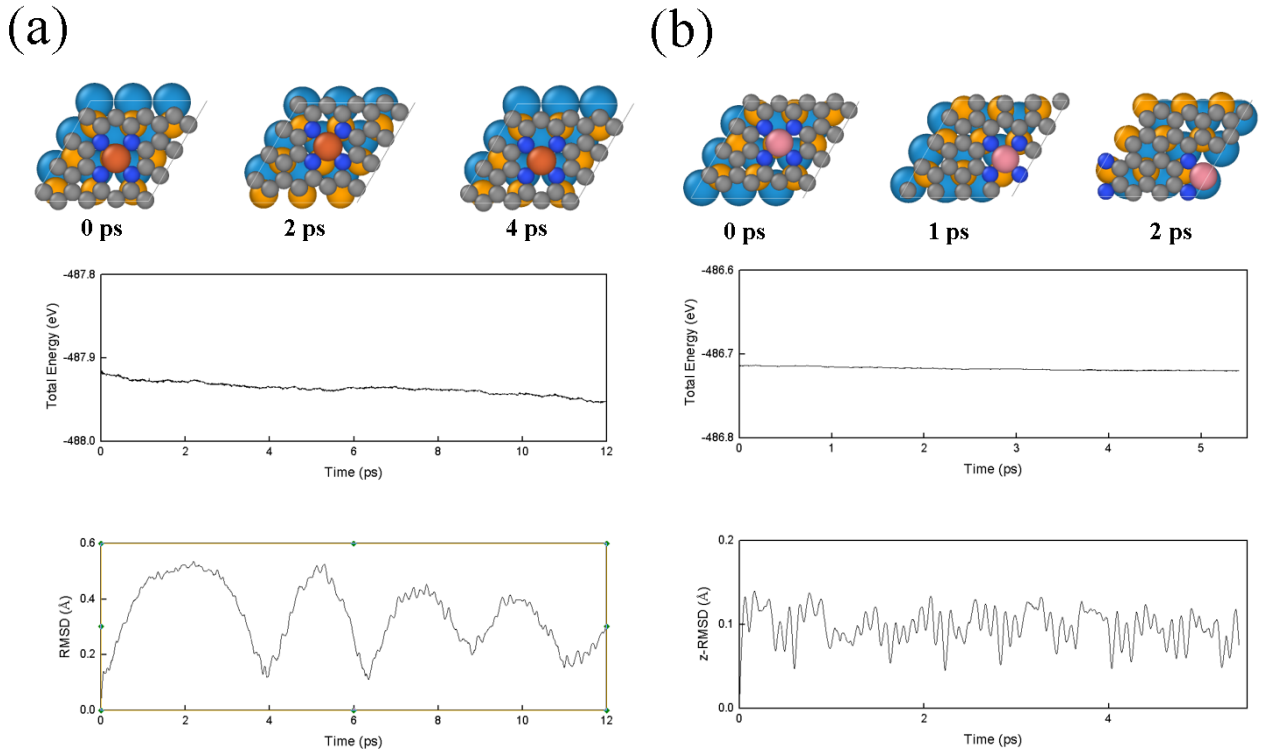

Fig. S2 MD simulations for **(a)** FeN_4@WSe_2, and **(b)** CoN_4@WSe_2.

6. Key elementary step and reaction barrier

O_2* + H^+ + e^- → OOH* is a suggested key step of common ORR. In the report of *J. Am. Chem. Soc.* **145**, 25352–25356 (2023), the step O_2 + * → O_2* was found to be rate-limiting step. In aqueous environment, one H_2O molecule pre-coordinates with Fe. In the beginning of ORR, O_2 should conquer the barrier to replace H_2O. To reveal the barrier of key elementary step of ORR on MN_4@RX_2, climbing image nudged elastic band method was employed. Explicit water model was built by setting several H_2O molecules around MN_4. As an example, FeN_4@WSe_2 was studied to compare with FeN_4.

In aqueous environment, one H_2O coordinates with Fe and occupies the catalytic site. During O_2 adsorption, the H_2O molecule is replaced (see **Fig. S3(a)**). On pristine FeN_4, the barrier of the step O_2 + * → O_2* is 0.96 eV. In FeN_4@WSe_2, the electrons of the Fe center are slightly taken away by the WSe_2 substrate, which benefits O_2 adsorption. **Fig. S3(b)** plots the energy profile of O_2 adsorption on pristine FeN_4 and

FeN_4@WSe_2. On FeN_4@WSe_2, the barrier of the step $O_2 + * \rightarrow O_2*$ is 0.54 eV, which is lower than that on pristine FeN_4.

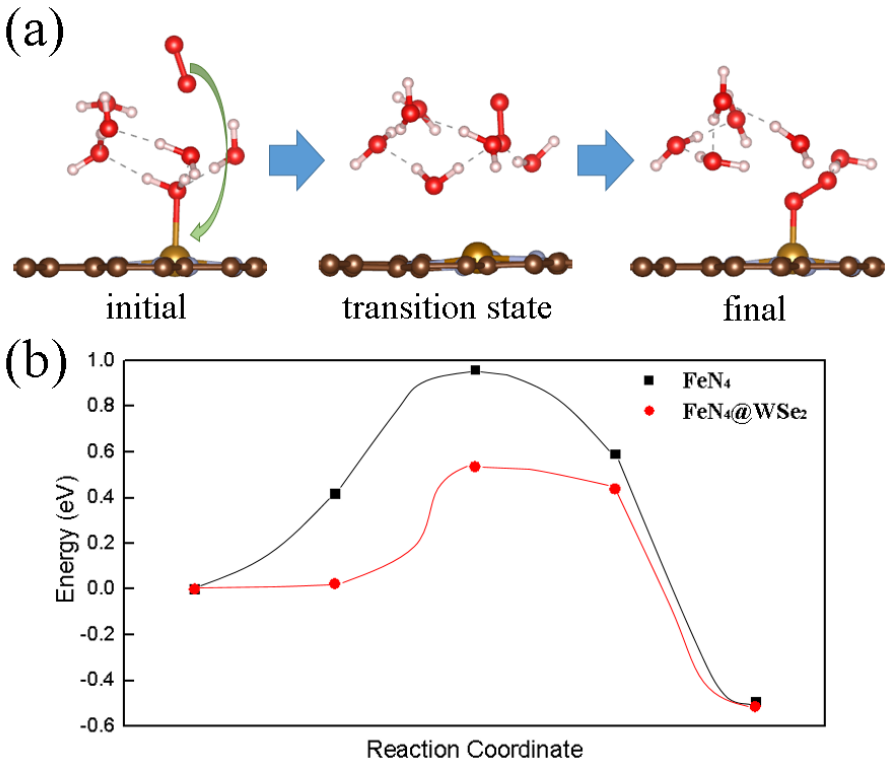

Fig. S3 (a) The structure evolution and **(b)** energy profile of O_2 adsorption on pristine FeN_4 and FeN_4@WSe_2 in water environment.

To investigate the $O_2* + H^+ + e^- \rightarrow OOH*$ step on FeN_4, we note that the FeN_4 site is unstable under acidic conditions but stabilized in alkaline environments. Therefore, we studied the corresponding alkaline reaction $O_2* + H_2O + e^- \rightarrow OOH* + OH^-$. In this process, the OH^- product is stabilized by hydrogen bonding with surrounding water molecules. The proton from H_2O is transferred to the adsorbed O_2* via a proton relay chain ($O_2*\cdots(H_2O)_n\cdots H_2O \rightarrow OOH*\cdots(H_2O)_n\cdots OH^-$), resulting in the formation of OH^- at a distal water molecule. **Fig. S4(a)** shows the structures of initial, transition and final states (the arrows show the proton transfer). **Fig. S4(b)** plots the energy profile of $O_2* + H_2O + e^- \rightarrow OOH* + OH^-$ on pristine FeN_4 and FeN_4@WSe_2. On FeN_4@WSe_2, the barrier is 0.15 eV, which is lower than that on pristine FeN_4 (0.27 eV).

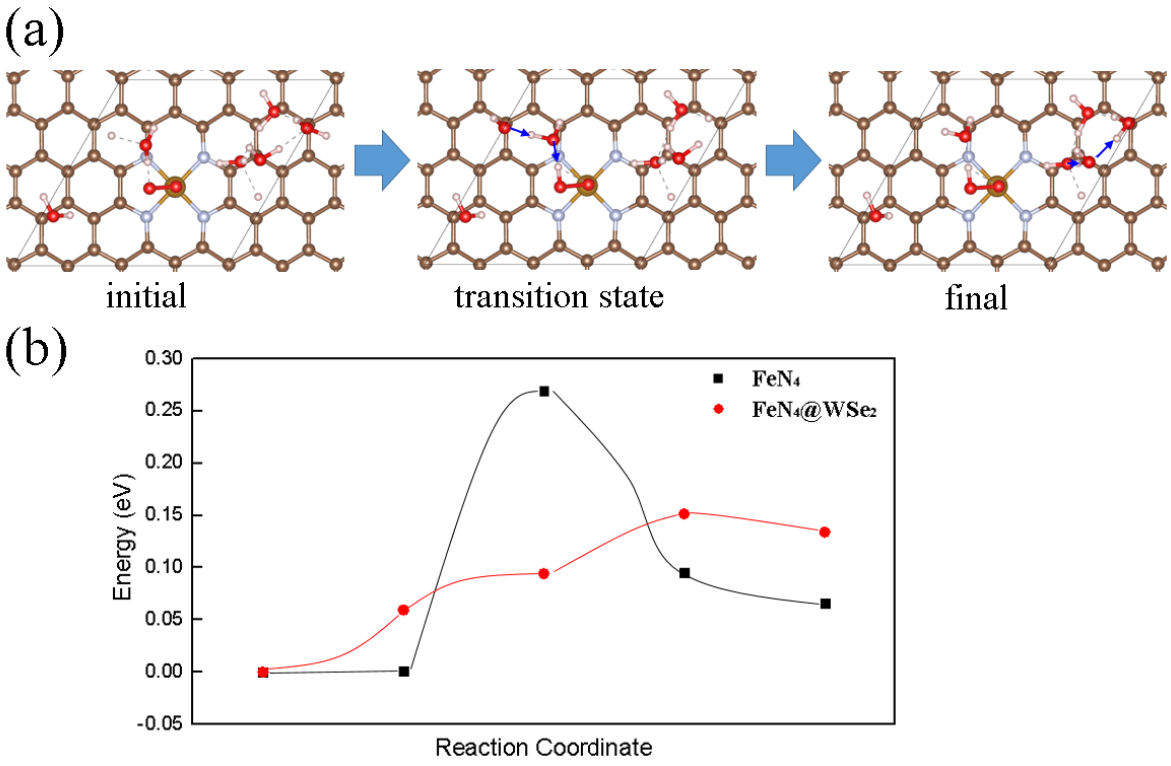

Fig. S4 (a) The structure evolution and **(b)** energy profile of O_2* + H_2O + e^- → OOH* + OH^- on pristine FeN_4 and FeN_4@WSe_2 in water environment.